

**Target Identification and Detection using LWIR Hyperpectral Signature Transformation of  
Multiple Missions without Registration**

Rulon Mayer<sup>a</sup>, Richard Priest<sup>b</sup>

<sup>a</sup> SFA, Woodlands Office Center, 9315 Largo Drive West, Suite 200, Largo, MD 20774

<sup>b</sup> Optical Sciences Division, Naval Research Laboratory, 4555 Overlook Ave., SW  
Washington DC 20375-5320

**ABSTRACT**

Changes in atmospheric conditions and sensor response for successive imaging sessions have limited the use of fixed target hyperspectral libraries, especially for multiple mission studies, to help identify and discriminate targets from cluttered backgrounds. The hyperspectral target signature instability has resulted in a dependence on anomaly detection algorithms in real time surveillance applications. These algorithms fail to meet some critical military requirements. This study examines a variety of mathematical transforms of the spectral signatures derived from missions flown on different days with starkly different weather conditions. The transforms use overlapping regions in the two data sets but avoid registering the image cubes. Some of the transforms use statistical features such as auto covariance matrices, means, and/or standard deviations of the image cubes. Other algorithms use spectral means taken from common features in the image cubes such as trees, roads, or blackbodies in both image cubes. Our study examines target spectra transformations in the long-wave infrared spectra of man-made targets and natural backgrounds obtained with the SEBASS (8-12  $\mu$ m) imager as part of the Dark HORSE 2 exercise during the HYDRA data collection in November, 1998. This study computes the signal to clutter ratio (SCR) for transforms that required high accuracy registration, various spectral signature transformations that do not need any registration, and those transforms that used random, varying number of pixels in the overlap area. The transformed signatures were subsequently used in matched filter searches to successfully find targets with low false alarm rates ( $< 1$  FA/Km<sup>2</sup>). Transforms that use covariance matrices from the image cubes achieve significantly higher performance relative to those algorithms that use spectral libraries of common features in the image cubes or rely on the image cube means. However, transforms that use covariance matrices (rather than image cube means or spectral libraries) require greater overlap in the area coverage of the two image cubes to achieve maximal SCR. Mathematically transformed spectral signatures can dramatically improve detection performance.

20010503 004

## 1. INTRODUCTION

Recently [1] there has been interest in using multiple missions over extended time periods to remotely detect targets. Spectral signatures derived from a multispectral or hyperspectral imager can be used in matched filter algorithms to help discriminate targets from cluttered backgrounds. Unfortunately, a given spectral signature may not remain stable during subsequent flight missions due to changes in atmospheric conditions and sensor response [2-3], thus limiting target detection using a matched filter algorithm. This study mathematically transformed spectral signatures from one day to another and then used these transformed signatures in matched filter searches for targets.

Previous studies [2],[3] examined the evolution of the spectral signatures over several missions. This earlier work found that data collected on a given day were stable and required no additional corrections. Spectral signatures, for subsequent days, changed more due to changes in atmospheric conditions and sensor response. Image-based corrections of the spectral signatures performed better than those based solely on atmospheric corrections. Image based corrections accounted for the effects of the changes of the atmosphere and sensor response on the spectra between missions. The best image-based correction, known as chronochrome [4], is derived from minimizing errors from a linear scaling matrix but requires sub-pixel registration. Registration of image cubes, difficult under the best conditions, is further complicated by the presence of uncorrected roll, and the inability to fly multiple missions that exactly track each other.

Earlier studies addressed some of the issues examined in this work. Considerable effort has been devoted to correcting for the intervening atmosphere between the remote sensor and the ground. For example, scene spectra have been normalized using an average-scene spectrum [5], using calibration panels in the scene ("empirical line method") [6], or using spectral features in the scene to autonomously search for specific objects such as green vegetation or blackbodies [7]. Alternatively, narrow detected features in the spectrum have been used to infer the integrated water amount within each pixel to deduce the content of other attenuating molecules and aerosols and to compute the scattering and transmittance of radiation [8]. Another approach uses a vast library of atmospheric conditions to account for changes in upwelling and transmittance, and then shrink the vast array of possible solutions to a smaller subspace of atmospheric conditions to help transform spectral signatures [9].

Other workers have focused on methods to approximate the autocovariance matrix to help identify objects and classify the image set. For example, as part of an effort to develop an adaptive anomaly detector, earlier studies [10] exploited information on the spatial and spectral correlation in the data set to help model the clutter and approximate the autocovariance matrix using only a few parameters. The problem of limited training data and approximations to the covariance matrix has also been examined. Previous investigators [11-13] reduced the number of pixels in the image cubes and approximated the auto-covariance matrix so as to avoid problems involving matrix singularity issues and to help segment the image set.

The present work examines the ability to mathematically transform spectral signatures of targets viewed during multi-temporal monitoring studies (Figure 1). The goal is to develop and test algorithms that do not require registration between the image cubes. Our primary interest lies in studying the effectiveness of a variety of methods in improving target detection capabilities. These new transforms convert target signatures from one day to another day and use these altered signatures in matched filter searches. The transformed signatures were compared with those signatures converted with the chronochrome transform and with the unchanged in-scene signature. The new transforms approximate the cross-covariance matrix, the only component in the chronochrome algorithm that depends on registration. All transforms were tested in terms of stability and ability to detect targets by varying the number of randomly sampled pixels in the "Target" image cube. These transforms were examined by comparing ROC curves (plots of the probability of target detection versus false alarm rate) using the converted target spectra for the matched filter algorithm.

## 2. SENSOR AND MISSION DESCRIPTION

The Dark HORSE 2 collection [14], which used the SEBASS sensor from Aerospace Corporation [15], flew on a Twin Otter airplane over Eglin Air Force base and imaged a set of prescribed scenarios with man-made targets and backgrounds composed of trees and roads. This study focuses on the data collected over three consecutive days (November 10, 11, 12, 1998). The SEBASS LWIR (long wave infrared radiation) sensor responds to thermal

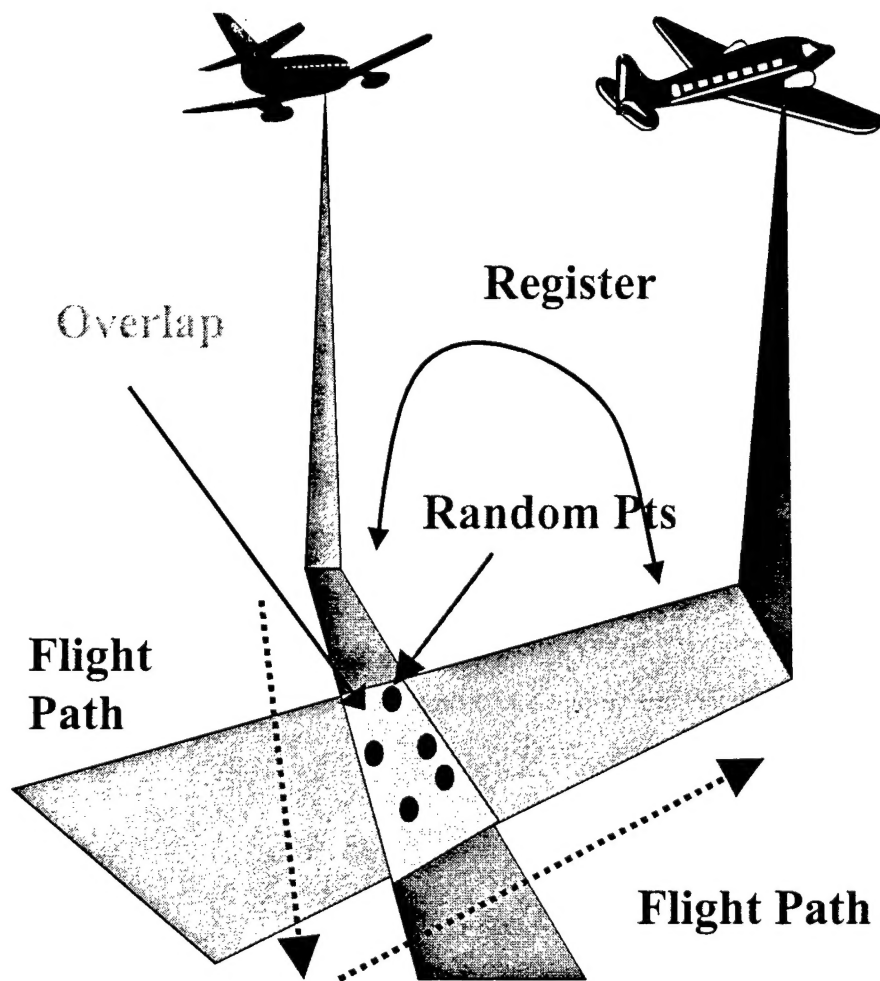


**Figure 1.** Schematic figure of multiple missions of remote hyperspectral imager and associated overlapping regions.

Registration between sets of missions means geometrically orienting and aligning each pixel in both missions.

radiation in the 7.8-13.4 micron region. The data were collected with a focal plane array (FPA) using 8 DSP digitizers (SHARC). The slit is 180  $\mu\text{m}$  wide and the optics between the slit and the FPA is arranged such that the image of the slit at the position of the FPA matches the pixel size of 75  $\mu\text{m}$ . The data were collected using the push broom technique at a nominal 30 Hz rate. The plane carrying the sensor flew at an elevation of approximately 850 meters above the targets. The hyperspectral data were acquired approximately once per pass during data runs (about every 6 - 10 min). In addition, flat field calibrations (intensity corrections at pixel level for the FPA using blackbody sources of LWIR radiation) were applied to the hyperspectral data and taken just prior (within 10 min, sometimes less) to the run. The imager was flat-fielded using temperature sources of approximately 20 and 40 C. Following spectral and spatial edge editing, the image cubes were binned to 30 bands spanning the LWIR range, with a cross track size of 128 pixels, and variable track length.

### 3. TRANSFORMATIONS: APPROXIMATIONS TO CHRONOCHROME

This study examines transformations of three dimensional image cubes composed of two-dimensional spatial arrays (labeled with a single subscript  $k$ ) and the other dimension associated with wavelength (labeled with superscript index  $i$ ). The chronochrome algorithm [4] uses a matrix  $C$  which is constructed so that the predictor  $C$  minimizes the mean squared error. Specifically,  $C$  can transform a given spectral signature or image cube  $x_1$  to another spectral signature or image cube  $x_2$  relative to their respective mean values i.e.

$$x_{2,k}^i - x_{2,\text{mean}}^i = \sum_j C_{21}^{ij} (x_{1,k}^j - x_{1,\text{mean}}^j) \quad (3.1)$$

$C_{21}^{ij}$  is derived from the component  $i,j$  in the mean square error  $\epsilon$  for  $N$  pixels in each image i.e.

$$\epsilon = \frac{1}{N} \sum_i \sum_{k=1}^N \{ ((x_{2,k}^i - x_{2,\text{mean}}^i) - \sum_p C_{21}^{ip} (x_{1,k}^p - x_{1,\text{mean}}^p)) ((x_{2,k}^i - x_{2,\text{mean}}^i) - \sum_q C_{21}^{iq} (x_{1,k}^q - x_{1,\text{mean}}^q)) \} \quad (3.2)$$

by minimizing the error with respect to  $C_{21}^{ij}$

$$\frac{\partial \epsilon}{\partial C_{21}^{ij}} = 0 \quad (3.3)$$

solving for  $C_{21}^{ij}$  results in

$$C_{21}^{ij} = \sum_m R_{21}^{im} (R_{11}^{-1})^{mj} \quad (3.4)$$

where  $R_{21}^{ij}$  is the cross covariance for bands  $i$  and  $j$  respectively or

$$R_{21}^{ij} = \frac{1}{N} \sum_{k=1}^N (x_{2,k}^i - x_{2,\text{mean}}^i) (x_{1,k}^j - x_{1,\text{mean}}^j) \quad (3.5)$$

and where  $R_{11}^{ij}$  is the auto covariance for the "non-target" regions or

$$R_{11}^{ij} = \frac{1}{N} \sum_{k=1}^N (x_{1,k}^i - x_{1,\text{mean}}^i) (x_{1,k}^j - x_{1,\text{mean}}^j) \quad (3.6)$$

Registration between image cubes  $x_1$  and  $x_2$  is needed to compute the cross correlation  $R_{21}$ . The missions were registered using common tiepoints in the image cubes under study. Spectral signature  $L_1$  from mission 1 is transformed to another spectral library appropriate  $L_{2,\text{trans}}$  for the conditions in mission 2 via

$$L_{2,\text{trans}}^i - x_{2,\text{mean}}^i = \sum_j C_{21}^{ij} (L_1^j - x_{1,\text{mean}}^j) \quad (3.7)$$

This study examined a variety of approximations to the cross covariance  $R_{21}$  that did not require registration: using the auto covariance associated only with mission 2 or  $R_{22}$  and the auto covariance associated only with mission 1 or  $R_{11}$  and standard deviations  $\sigma_1$ ,  $\sigma_2$  where

$$\sigma_h^i = \sqrt{\frac{1}{N-1} \sum_{k=1}^N \{x_{h,k}^i - x_{h,\text{mean}}^i\}^2}, h = 1, 2 \quad (3.8)$$

and means  $x_{h,\text{mean}}$  of individual data sets.

#### 3.1 Observations and Goals

This study investigated a wide variety of transforms. However, this paper only discusses a small subset of algorithms, namely those that yielded the highest target detection for constant false alarm rate. This study only examines calibrated data sets. Transforms that yield the best target detection for this particular data set, may not work in other situations such as those that are not gain corrected. The study assumes that only atmospheric or sensor changes between mission determine the spectral transforms. In other words, the transforms under discussion assume that missions can be connected to each other through a simple relationship between pairs of bands (see Section 3.3), rather than coupling a given band to the entire set of bands.

A goal for this study was to approximate the cross covariance matrix  $R_{21}$  using data taken from two image cubes, without having to register them. Figure 2a displays a row (seventh band corresponding to  $\lambda=9.095$  microns) the chronochrome cross-covariance matrix, or  $R_{21}$ ; the equivalent row for the auto-covariance for the “hazy day”, or “Bkg-Bkg CV” matrix, or  $R_{11}$ ; the equivalent row for the auto covariance for the “In-scene” image cube or “Trg-Trg CV”, or  $R_{22}$ .

The ensuing sections discuss the symmetries of the approximated transforms, and supply plausibility arguments in support of examining the proposed transforms rather than rigorous derivations. Signal to clutter calculations and target detection probability for a given false alarm rate (following matched filter searches using transformed signatures) provide the quantitative comparisons of the transforms in this study for the particular scenario studied.

### 3.2 Symmetries

The chronochrome algorithm uses the cross covariance matrix  $R_{21}$  and a predictor  $C_{21}$  to help transform spectral signatures. Under “time reversal” or interchange of the labels for the missions 1↔2, the cross covariance  $R_{21}$  and predictor  $C_{21}$  respond in certain ways. Approximations to the chronochrome algorithm, however, may or may not obey the same symmetries as the chronochrome. This study examined the approximated transform symmetry and correlated the ability of the transform to discriminate targets from backgrounds. From inspection, the cross covariance obeys the following symmetry namely

$$R_{21}^{ij} = R_{12}^{ji} \quad (3.9)$$

and the auto covariance matrices obey the following symmetries

$$R_{11}^{ij} = R_{11}^{ji} \quad (3.10)$$

and

$$R_{22}^{ij} = R_{22}^{ji} \quad (3.11)$$

In addition, if  $\epsilon^{ij}=0$ , then chronochrome predictor  $C_{21}$  follows

$$C_{21}^{ij} = (C_{12}^{ij})^{-1} \quad (3.12)$$

where

$$C_{12}^{ij} = \sum_m R_{12}^{im} (R_{22}^{-1})^{mj} \quad (3.13)$$

If however  $\epsilon \neq 0$ , then

$$C_{21}^{ij} \neq (C_{12}^{ij})^{-1} \quad (3.14)$$

A variety of approximations to  $R_{21}$  were proposed and tested. Table 1 lists the approximations to  $R_{21}$ . The behavior of the approximate transforms under interchange of missions 1 and 2 are also listed.

**Table 1**  
**List of Approximations to Chronochrome and**  
**Symmetries**

<b>R<sub>21</sub></b> <b>Approximation</b> <b>Type</b>	<b>R<sub>21</sub></b>	<b>R<sub>21</sub><sup>ij</sup>= R<sub>12</sub><sup>ji</sup></b>	<b>C<sub>21</sub><sup>ij</sup>= (C<sub>12</sub><sup>ji</sup>)<sup>-1</sup></b>
<b>Chronochrome</b>	$R_{21}^{ij}$	Yes	No
<b>Average CV</b>	$0.5\{R_{11}^{ij} + R_{22}^{ij}\}$	Yes	No
<b>Weighted CV</b>	$0.5\sigma_1^j\sigma_2^i \{(R_{11}^{ij}/\sigma_1^i\sigma_1^j) + R_{22}^{ij}/\sigma_2^i\sigma_2^j\}$	Yes	No
<b>Target CV</b>	$\sigma_1^j\sigma_2^i \{ R_{22}^{ij}/\sigma_2^i\sigma_2^j \}$	No	Yes
<b>Diagonal</b>	$\sigma_1^j\sigma_2^i \{ R_{11}^{ij}/\sigma_1^i\sigma_1^j \}$	No	Yes

### 3.3 Motivation for “diagonal” and “target” transform approximations to chronochrome

As a first approximation, suppose each pixel within image cubes 1 and 2 are related to each other simply as

$$x_{2,k}^i - x_{2,mean}^i \approx b_k^i (x_{1,k}^i - x_{1,mean}^i) \quad (3.15)$$

through a coupling coefficient  $b_k^i$ . This coupling coefficient can depend on the change in the intervening atmosphere transmission and changing sensor response between the two missions. Further, suppose  $b_k^i$  only depends on the wavelength or band number  $i$ , independent of pixel location  $k$  (i.e. image cubes have been flat-fielded, no clouds within images). Then

$$R_{21}^{ij} \approx \frac{1}{N} \sum_{k=1}^N b^i (x_{1,k}^i - x_{1,mean}^i) (x_{2,k}^j - x_{2,mean}^j) = b^i R_{11}^{ij} \quad (3.16)$$

and similarly

$$\sigma_2^i \approx \sqrt{\frac{1}{N-1} \sum_{k=1}^N (b^i)^2 \{x_{2,k}^i - x_{2,mean}^i\}^2} = (b^i) \sigma_1^i \quad (3.17)$$

After substituting for  $b^j$  and rearranging terms, the “background CV” or “diagonal” transform refers to the following expression

$$R_{21}^{ij} \approx \sigma_1^j \sigma_2^i \frac{R_{11}^{ij}}{\sigma_1^i \sigma_1^j} = R_{11}^{ij} \frac{\sigma_2^i}{\sigma_1^i} \quad (3.18)$$

If the quantities  $R_{11}$ ,  $R_{22}$ ,  $\sigma_1$ ,  $\sigma_2$  are directly taken from the image sets, then “time reversal” symmetry for the cross covariance  $R_{21}$  (i.e.  $R_{21}^{ij} \neq R_{12}^{ji}$ ) is not obeyed for the “diagonal” transform approximation. The latter approximation is referred to as “diagonal” because the approximate full chronochrome predictor  $C_{21}$  is then given by a diagonal matrix

$$C_{21}^{ij} \approx \frac{\sigma_2^i}{\sigma_1^i} \delta_{ij} \quad (3.19)$$

The predictor  $C_{21}$  for the “diagonal” transform obeys  $C_{21}^{ij} = (C_{12}^{ji})^{-1}$ .

The “diagonal” approximation is only one way to couple the image sets through a linear scaling coefficient. Another transform that strongly resembles the “diagonal” transform can be considered. In a similar fashion used in motivating the “diagonal” transform, suppose each pixel within image cubes 1 and 2 are related to each other

$$x_{1,k}^j - x_{1,mean}^j \approx \frac{1}{b_k^j} (x_{2,k}^j - x_{2,mean}^j) \quad (3.20)$$

through a coupling coefficient the inverse  $b_k^j$ . Again, suppose  $b_k^j$  only depends on the wavelength or band number  $j$ , independent of pixel location  $k$ . Then

$$R_{21}^{ij} \approx \frac{1}{N} \sum_{k=1}^N \frac{1}{b_k^j} (x_{2,k}^j - x_{2,mean}^j) (x_{1,k}^i - x_{1,mean}^i) = \frac{1}{b^j} R_{22}^{ij} \quad (3.21)$$

and similarly

$$\sigma_1^j \approx \sqrt{\frac{1}{N-1} \sum_{k=1}^N \left(\frac{1}{b^j}\right)^2 \{x_{1,k}^j - x_{1,mean}^j\}^2} = \left(\frac{1}{b^j}\right) \sigma_2^j \quad (3.22)$$

After substituting for  $b^j$  and rearranging terms, the “target CV” transform refers to the following expression

$$R_{21}^{ij} \approx \sigma_1^j \sigma_2^i \frac{R_{22}^{ij}}{\sigma_2^i \sigma_2^j} = R_{22}^{ij} \frac{\sigma_1^i}{\sigma_2^j} \quad (3.23)$$

Under “time reversal”, the predictor associated with the “target CV” transform follows  $C_{21} = (C_{12})^{-1}$ .

### 3.4 Motivation for “weighted CV” Transform

The “diagonal” and the “target CV” transforms assume that the image cubes for missions 1 and 2 are connected to each other through a coupling coefficient, independent of position in the image. Thus, both approximated transforms do not follow the expected behavior of the exact chronochrome algorithm under interchange of labels 1 and 2. “Weighted CV” is a symmetrized combination of the “diagonal” and “target CV” transforms i.e.

$$R_{21}^{ij} = \sigma_1^j \sigma_2^i (.5 \frac{R_{11}^{ij}}{\sigma_1^i \sigma_1^j} + .5 \frac{R_{22}^{ij}}{\sigma_2^i \sigma_2^j}) \quad (3.24)$$

The item inside the parenthesis may be interpreted as an average of the correlation coefficients for missions 1 and 2. Interchange of mission labels 1 and 2 for the “weighted CV” version of  $R_{21}^{ij}$  results in  $R_{21}^{ij} = R_{12}^{ji}$  and the predictor  $C_{21} \neq (C_{12})^{-1}$ . The “weighted CV” transform matches the symmetry of the chronochrome transform under interchange of labels 1 and 2.

### 3.5 Motivation for “average CV” Transform

This study simulates the Chronochrome predictor  $C_{21}$  through approximating the cross covariance matrix  $R_{21}$ . If the overlap regions within data sets 1 and 2 are calibrated and have not changed substantively then it may be possible to examine to assume that  $\sigma_1 = \sigma_2$  for all spectral components, then the “weighted CV” simplifies to the “average CV” or

$$R_{21}^{ij} = .5(R_{11}^{ij} + R_{22}^{ij}) \quad (3.25)$$

Figure 2a shows that a row in the cross covariance  $R_{21}$  matrix lies between the appropriate rows in the auto covariance matrices  $R_{11}$  and  $R_{22}$ . The “average CV” transform matches the symmetry of the chronochrome transform under interchange of labels 1 and 2. In addition, the approximation to  $R_{21}$  obeys an additional symmetry namely  $R_{21}^{ij} = R_{12}^{ji}$  and  $C_{21} \neq (C_{12})^{-1}$ .

## 4. Transformations: Background Spectral Features: Scaling and Offset Transforms

### 4.1 Scaling-based Techniques

This study also examined simpler approaches that did not require minimizing the predicted error. Instead, it is assumed that a particular “typical” or “representative” feature, identified and detected in both image cubes, provides a valid indicator of changes for all pixels in the overlap region. The alternative approach for predicting spectral signatures assumes that differences in the image sets may be due to changes in atmospheric transmission and/or sensor response, but does not depend on pixel position. In addition, it is further assumed that the predictor is diagonal and changes in the spectra follow a **scaling** type of transform

$$(x_{2,k}^i - x_{2,mean}^i) \approx C^{ii} (x_{1,k}^i - x_{1,mean}^i) \quad (4.1)$$

Equation 4.1 is identical to equation 3.15 but different labeling is used to help distinguish the two very different approaches for transforming the target spectra. This study instead uses common features, identified by the image analyst in the two sets such as trees or sandy roads or automatically identifies “blackbodies” using the ISAC algorithm [15] or computes the means in the two image sets. In other words, the average spectrum  $X_{Ave\_Spec}$  for trees, or sandy roads, or blackbodies are substituted for  $x_{2,k}^i$  and  $x_{1,k}^i$ .

$$X_{2,Ave\_Spec}^i - x_{2,mean}^i \approx C^{ii} (X_{1,Ave\_Spec}^i - x_{1,mean}^i) \quad (4.2)$$

where  $X_{Ave\_Spec}^i$  is the average spectrum  $X_{Ave\_Spec}$  for the trees, sandy road, blackbody. The full approximate chronochrome predictor is diagonal and given by

$$C^{ii} \approx \frac{X_{2,Ave\_Spec}^i - x_{2,mean}^i}{X_{1,Ave\_Spec}^i - x_{1,mean}^i} \quad (4.3)$$

Presumably the common features (trees, sandy roads, blackbodies) follow the median values of image cubes i.e.

$$\sum_k x_k^i \propto x_{mean}^i \quad (4.4)$$

and so the predictor can be further simplified as

$$C^{ij} \approx \frac{X_{2,Ave\_Spect}^i}{X_{1,Ave\_Spect}^i} \delta_{ij} \quad (4.5)$$

The latter expression for the predictor depends solely on the average spectra and does not contain any explicit information regarding the statistics of the image cubes. This expression is similar to the automatic scene-adaptive techniques used in ERIM algorithm [16] for transforming spectral image libraries.

The scaling predictions and approximations  $C^{ij}$  are used to transform the spectra  $L_1$  of a target taken from the initial image cube (in this study, “hazy day” image cube) to the transformed target spectra  $L_{2,trans}$  to be used in the matched filter search.

$$L_{2,trans}^i = C^{ii} (L_1^i - x_{1,mean}^i) + x_{2,mean}^i \quad (4.6)$$

#### 4.2 Offset-based Techniques:

Instead of using the scaling transformation to predict changes in the two image cubes (such as in the chronochrome approach), this study also examined offset vectors. The offset mapping follows

$$(x_{2,k}^i - x_{2,mean}^i) \approx (x_{1,k}^i - x_{1,mean}^i) + B^i \quad (4.7)$$

Applying the same considerations, assumptions, and substitutions used in the simplified scaling approach, namely assuming that a “typical” spectral feature  $X_{Ave\_Spect}$  (identified by an image analyst or automatically detected) the offset predictor  $B^i$  follows

$$B^i = (X_{2,Ave\_Spect}^i - x_{2,mean}^i) - (X_{1,Ave\_Spect}^i - x_{1,mean}^i) \quad (4.8)$$

Common background objects in the scene ( $X_{Ave\_Spect}$  such as trees, sandy road, “blackbodies”) are used to convert the target spectral signature through an offset correction i.e.

$$L_{2,trans}^i = L_1^i + (X_{2,Ave\_Spect}^i - X_{1,Ave\_Spect}^i) \quad (4.9)$$

This correction is then applied to all spectra under study and is labeled as **Offset**.

## 5. MISSION SUMMARY

The missions were flown at night (Day 3 or “Target” or “In-Scene” or Mission 3, shot #27 according to [14] nomenclature) and early dawn (Day 1 or Background or “Hazy Day” or Mission 5, shot #13 according to [14] nomenclature). The relative humidity varied from to 100% (Day 1) to 85% (Day 3). The air temperature ranged from 14.5 C (Day 1) to 5.5 C (Day 3). The image data were collected at an elevation of 850 meters and the sensor was oriented in the nadir direction. The target mission was flown in the easterly direction while the background was flown in the northerly direction. The overlapping region was small relative to the entire data set. For the chronochrome transform, the images were linearly rotated, translated, and resampled and registered (to 0.3 pixel) using 8 tie-points.

## 6. RESULTS

Figures 2b shows a row  $R_{21}$  (specifically the seventh band or  $\lambda=9.096$  microns) from the chronochrome algorithm as well as the appropriate row taken from approximations to the cross covariance matrix including the “average CV”, “weighted CV”, “diagonal”, and “target CV”. An examination of all of the rows and columns (not only the row shown in Figure 2b) of the cross covariance matrix, finds that the “average CV”, and “weighted CV” most closely resemble the values derived using chronochrome, over the entire wavelength or band.

The man-made targets were distributed in the viewing area and are designated as target type #1, target type #2, and target type #3. The computed signal to clutter ratio (SCR) of the target types #1, #3 signature following

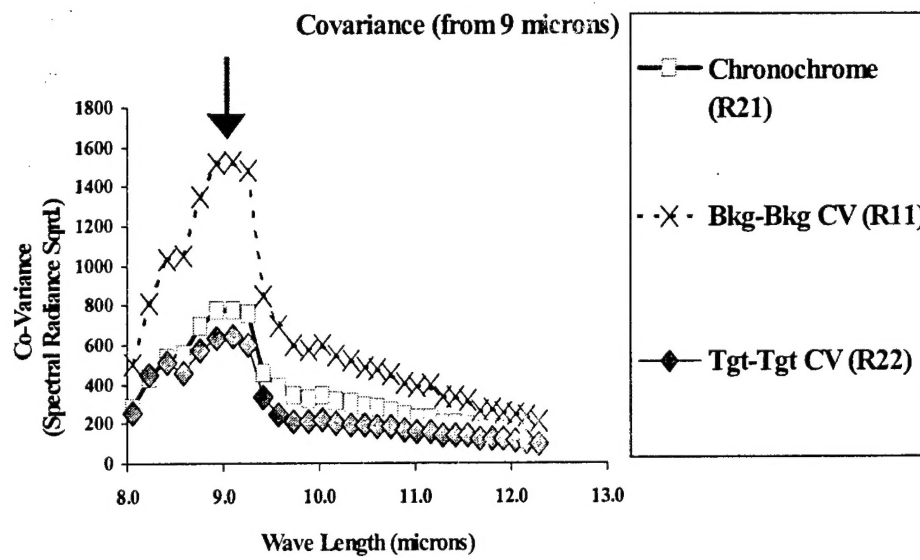


**Figure 2a.** The displayed cross covariance profiles are individual rows taken from the cross covariance matrix. The labels denote the cross covariance (chronochrome), Unit CV, auto covariance for the Background Bkg-Bkg CV, Target Tgt-Tgt CV, Bkg-Bkg CV. In all the displayed profiles show a particular row (Band 7, or wavelength 9.096 microns). Arrow shows reference band 7 or wavelength 9.096 microns.

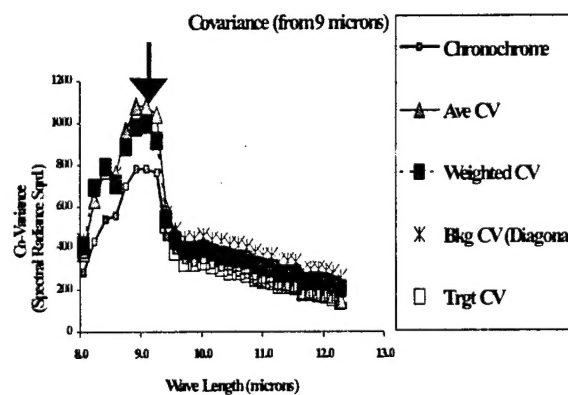


**Figure 2b.** Approximations to cross covariance profiles are the cross covariance (chronochrome), Average CV, Weighted CV, Bkg CV (Diagonal). In all the displayed profiles show a particular row (Band 7, or wavelength 9.096 microns). Arrow shows reference band 7 or wavelength 9.096 microns.

transformation by the labeled algorithms is displayed in Figures 3 and 4. The SCR in this study (see Equation 11 in [3]) is computed from the ratio of the target contrast relative to the background variance. The SCR calculation treats the “in-scene” signature ( $L_{2\text{-}x}_{2,\text{meas}}$ ) as the target signature and the transformed signature vector ( $L_{2,\text{trans-}x}_{2,\text{mean}}$ ) is used within a Weiner Filter projection [2,3]. SCR from unaffected (raw, unconverted) spectra are also displayed to provide a reference to the maximum SCR and labeled as “in-scene limit” ( $\text{SCR}_{\text{Ref\_Max}}$ ). The “in-scene” target spectrum  $L_2$  is taken from the Mission 2 image cube. The “hazy day limit” is the SCR computed using the uncorrected target spectrum  $L_1$  taken from the Mission 1 or “hazy day” image cube. From the figures, it can be seen that algorithms which more closely match the chronochrome predictor (“weighted CV”, “average CV” see figure 2b) achieve larger computed SCR relative to those that depart from the chronochrome algorithm (figures 3a, 4a). Similarly, figures 3b, 4b show the SCR from algorithms that scale and offset spectra of features in the clutter (such as roads, trees, blackbodies, clutter mean) to transform target spectra (see Section 4). Algorithms that only scale or offset individual spectra (figures 3b, 4b), show lower SCR relative to those that use statistics that characterize the entire clutter in the overlap region (figures 3a, 4a). Transforms that use offset to correct target signatures show very similar behavior to the behavior shown using the scaling approach (figures 3b, 4b). Although only two types of target spectrum (Target #1, Target #3) are shown, calculations (again, not shown due to manuscript length limitations) demonstrate that transformations of the other target spectra (Target #2) show the same trend displayed in figures 3 and 4. Specifically, all targets (Target #1, #2, #3) achieve larger SCR using clutter statistics (discussed in Section 3) relative to those that only use individual spectra (see Section 4).

This study also tested the stability of the transformation algorithms. As a starting point, a limited, randomly distributed number of pixels, in the target (“In-Scene”) image cube were used in the calculations. The coverage ranged from 0.1% (or 10 pixels) up to 100% (100,000 pixels). SCR as a function of pixel number for approximations to the chronochrome matrix are shown figure 5a. The reduction in the number of pixels (and coverage) diminishes sampling of the clutter (figure 5a). The poorer sampling degrades the SCR for a given algorithm. Using fewer sampling pixels also increases the statistical uncertainty (each of the random sample were run four times) (figure 5a). For coverages exceeding 5% and 500 pixels, the response appears insensitive to pixel number. To avoid problems with singularities, inverted covariance dependent algorithms (i.e. chronochrome) sampled a minimum of 50 pixels (exceeding 30 or the number of wavelength bands). Tested algorithms that use the “In-scene” auto-covariance matrix (“average CV”, “weighted CV”) are most affected by the reduced sampling. Other algorithms that depend only on the standard deviation or means (“diagonal”) are far less sensitive to the number of sampled pixels and coverage and have lower statistical errors. However, these more stable algorithms also yield lower SCR relative to approximations based on chronochrome.  $\text{SCR}_{\text{Ref\_Max}}$  and “hazy day limit” SCR are also shown. Algorithms that only scale individual spectra (figure 5b), show lower SCR but more stable SCR for reduced number of pixels in the overlap region relative to those that use statistics that characterize the entire clutter in the overlap region (figure 5a). Again, transforms that use offset to correct target signatures show very similar behavior to the behavior shown using the scaling technique. Although only one type of target spectra is shown, additional calculations demonstrate that transforms of other types of targets show the same trends displayed in figures 5a and 5b. That is, less stable SCR using fewer number of pixels in the overlap region, are achieved for all target types (Targets #1, #2, #3) using clutter statistics (Section 3) relative to those that only use individual spectra (Section 4).

A false colored image showing clutter and the targets types #1, #2, #3 is shown in Figure 6a. Output from an anomaly search [17] applied to the same “In-scene” image cube is shown in Figure 6b. Strong signals from target types #1, #2, #3 are detected as well as false alarms from the clutter. Figure 6c shows output from the matched filter algorithm [18] applied to the “In-scene” image cube using the spectra from the transformed (“weighted CV” sampled with 1000 pixels or 10% coverage) Target #1 material. All objects associated with target type #1 are detected as well as a small signal from target type #3 as shown in Figure 6c. Figure 6c shows no signal from target type #2. Ground truth reveals that the target type #3 is permeable material that covered target type #1, and so that target type #1 signature leaks through the target type #3 material.

ROC curves (Figures 7a, 7b) (probability of target detection versus false alarm rates) assess the ability of transformed spectra to discriminate targets from clutter within the matched filter algorithm. Positive target detection at a given pixel is identified when the algorithm output exceeds a threshold value and the pixel resides inside a target. The targets are identified as aggregated objects. The targets in this analysis included one (target type #3) which actually showed remnants of Target #1. In contrast, false alarms are recorded for pixel values that exceed a threshold but also reside outside the identified target. Figure 7a shows the ROC curves for matched filters using

### Target Type #1 SCR

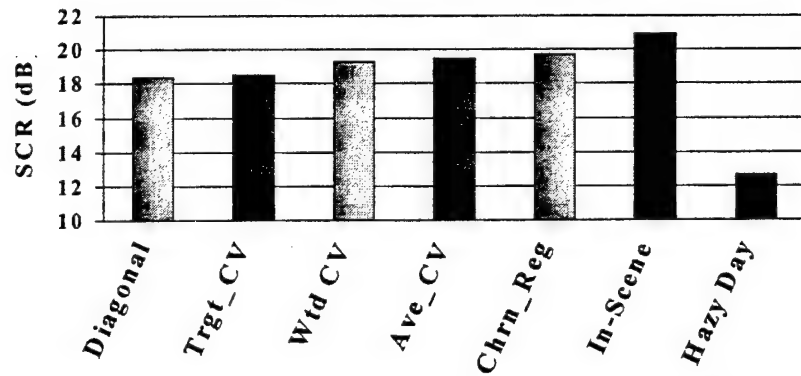


**Figure 3a** Chart showing SCR of Target #1 transformed via algorithms labeled as Chronochrome, Bkg CV (Diagonal), Tgt CV, Wtd CV, Ave. CV. Limits labeled as In-scene and Hazy-Day. SCR used cluttered data from In-scene image set.

### Target #1, SCR

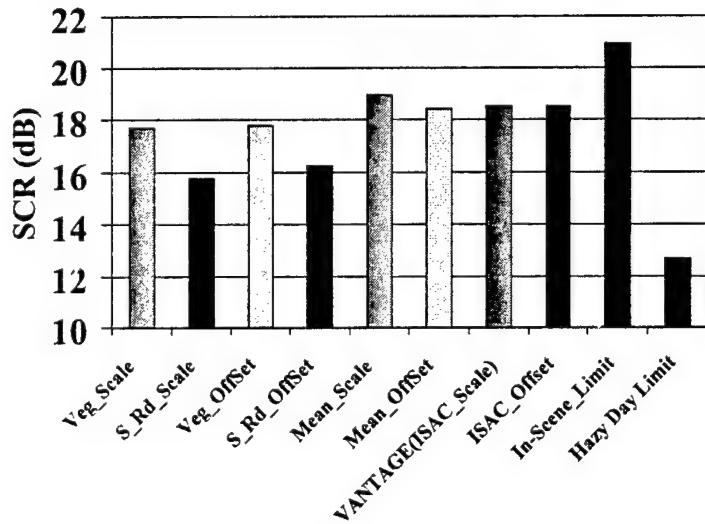


**Figure 3b** Chart showing SCR of Target #1 via transformations by algorithms using the offset, and scaling approaches. Labeled algorithms as tree, sandy road, ISAC. SCR limits indicated by In-scene, Hazy-day. SCR used In-Scene image set.

### Target Type #3 SCR

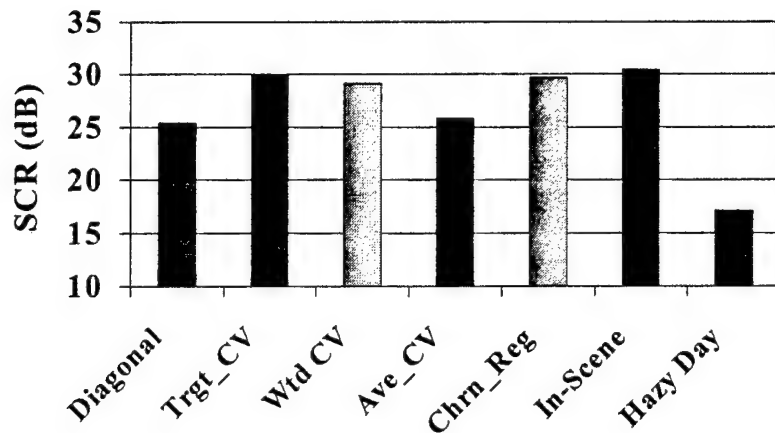


**Figure 4a** Chart showing SCR for Target #3 using algorithms labeled as Chronochrome, Diagonal, Target CV, Weighted CV, Average CV. Limits labeled as In-scene and Hazy day. SCR computed using In-Scene image set.

### Target #3, SCR

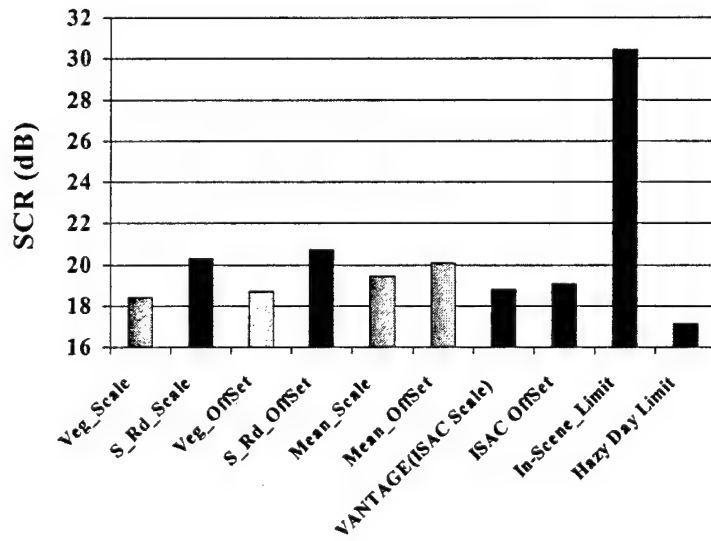


**Figure 4b** Chart showing SCR for Target #3 following transformations by algorithms using the offset, and scaling approaches. These transforms labeled as tree, sandy road, ISAC. Limits labeled as In-scene and Hazy day. SCR used clutter from In-Scene image set.

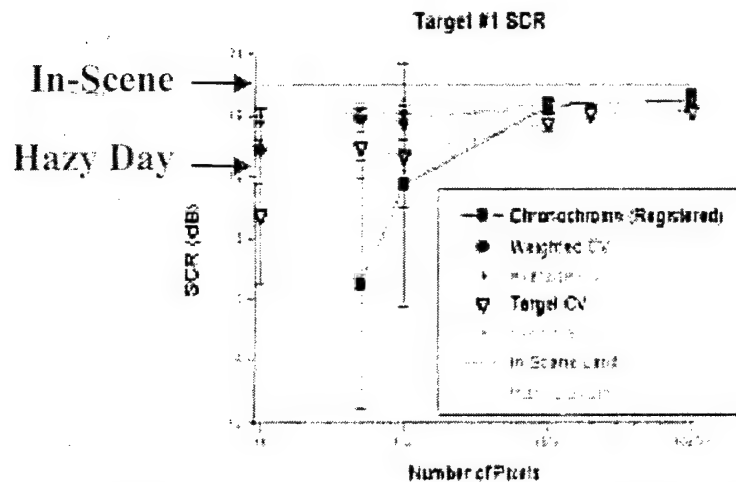


**Figure 5a** SCR as a function of number of randomly sampled pixels in the overlap region. Spectral libraries following Chronochrome, Weighted CV, Average CV, Target CV, Diagonal transforms of Target #1 spectra. SCR calculation uses “In-scene” (or target) image set. Uncorrected “In-scene” and “Hazy Day” spectra of Target #1 also displayed. Statistical error bars are shown.

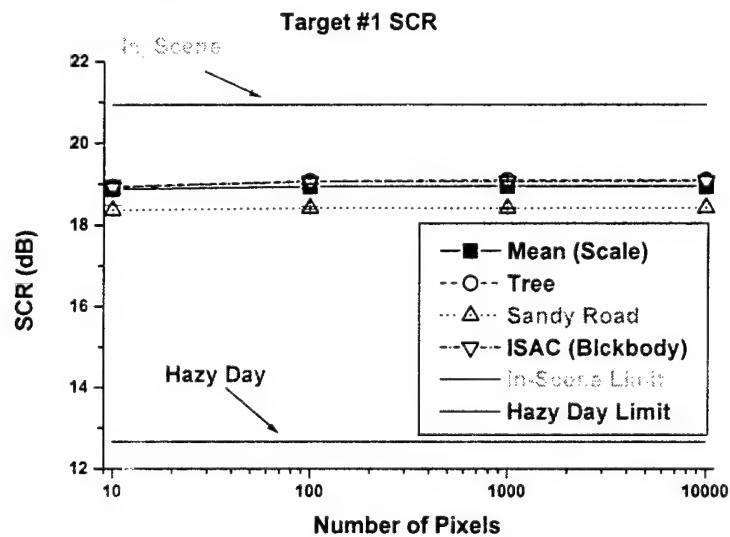


**Figure 5b** SCR as a function of number of randomly sampled pixels in the overlap region. Spectral libraries using Scaling approach and substituting Mean values, and averages of Trees, Sandy Road, Blackbody from ISAC spectra (the latter corresponds to VANTAGE). SCR calculation uses “In-scene” (or target) image set. Uncorrected “In-scene” and “Hazy Day” spectra of Target #1 also displayed. Statistical error bars are shown. Offset approach yields similar data.

target signatures from chronochrome, "average CV", "diagonal", the uncorrected "hazy day" target signature, and the anomaly search. The chronochrome, "average CV", and "weighted CV" (but not shown in Figure 7a) transformed signatures for matched filter searches can generate 100% target detection with zero false alarms. Matched filter algorithm using transforms that most faithfully resemble the chronochrome transform ("weighted CV", "average CV") yield large SCR for all target materials, and generate higher detection probabilities (for a fixed false alarm rate). Figure 7b shows that reducing the pixel number in the transformation (specifically the "weighted CV", but is valid for all other transforms) can diminish target detection as well as SCR. As suggested by the studies of SCR (figure 5a), excellent ROC curve performance can be achieved with relatively few pixels.

## 7. DISCUSSION

The chronochrome methodology to transform target signatures yields an excellent response as expressed in the ROC curves for matched filter applications in this analysis and other studies [2-3]. In addition, this technique generates large SCR in the particular scenarios under study. Chronochrome requires a pixel to pixel comparison and uses tie-points to help register two sets of spectral images derived from multiple flight missions. Registering independent image cubes is often time and computationally consuming and requires substantial intervention by an image analyst. For the scenarios examined in this study, the "diagonal", "target CV", "weighted CV", and "average CV" approximations to the chronochrome algorithm simultaneously provide faithful spectral library conversions for multi-temporal monitoring projects, and accurately detect targets amid the clutter in matched filter searches. In addition, the "diagonal", "target CV", "weighted CV", and "average CV" only require identification and association of overlapping areas but do not require precise registration. Further, for the scenarios considered in this study, these approximations are robust, generating valid transformations using relatively few pixels and low overlap coverages. The relative ability of the mathematical transforms to precisely convert the spectra is independent of the target material.

Algorithms that use spectral libraries of common features in the image cubes or rely on the image cube means generate lower SCR relative to transforms that use covariance matrices from the image cubes (compare figures 4a and 4b). However, transforms based on spectra of features found by an image analyst, extracted autonomously using the ISAC procedure, and/or using image cube means, are far less dependent on the number of pixels sampled or areal coverage (figure 5). Under low sampling conditions (<500 pixels, <0.5% coverage), these algorithms exceed covariance based transforms. Choice of particular features (roads, trees, blackbodies, image means) did not affect algorithm performance (as measured through SCR). In addition, selecting offset or scaling (of spectral features) to correct target spectra does not significantly affect algorithm performance. The scaling or offset-based algorithms are computationally simple and fast because they did not require computation of covariance matrices.

For this particular LWIR data set, the "weighted CV" and "average CV" transforms perform better than the "diagonal" and "target CV" transforms as indicated by SCR and the ROC curves. Unlike "diagonal" and "target CV" transforms, the cross covariance approximated by the "weighted CV" and "average CV" transforms follow the same symmetry under interchange of missions 1 and 2 as the chronochrome algorithm (see Table 1). The symmetry behavior of the cross covariance matrix may be an important criterion for selecting optimal transforms. Other candidate algorithms were tested (but not discussed in this paper) such as  $R_{21}^{-1} = \sigma_1^{-1} \sigma_2^{-1}$ , which follows the chronochrome behavior under interchange of missions 1 and 2, but suffers from reduced SCR and low target detection probability.

Due to varying conditions in other investigations, this study does not definitively endorse a particular spectral signature transform. For example, the image sets 1 and 2 discussed in this paper used calibrated, flat-fielded image sets. Due to the use of calibrated image sets in this project,  $\sigma_1 \approx \sigma_2$  and therefore the average CV offers an accurate, robust spectral signature (see figures 2b, 3a, 4a). However, the average CV may not provide an accurate signature transform for other image cubes that use uncalibrated image sets, or use image sets requiring gain corrections where  $\sigma_1$  differs substantially from  $\sigma_2$  for all bands. Differing conditions that prevail in other works can change the relative merits of the signature transforms proposed in this study.

Matched filter searches can specifically identify targets. However, matched filter algorithm searches are rarely used to find man-made targets within cluttered backgrounds due to unstable spectral signatures. Most studies apply

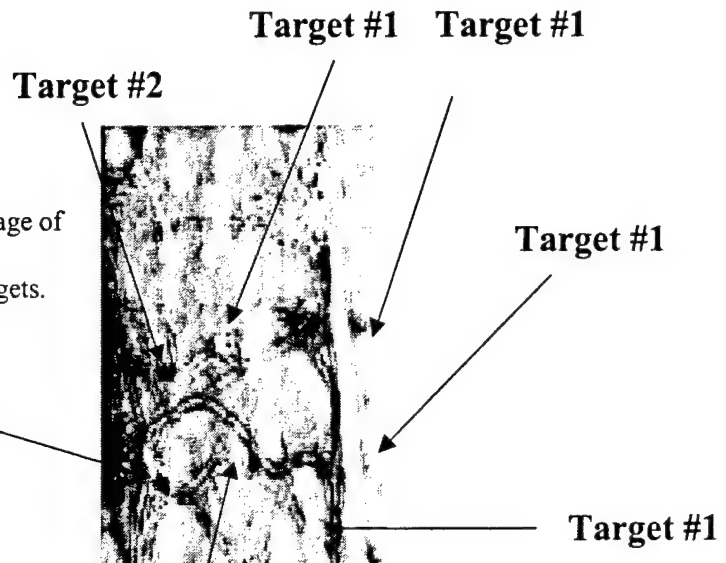


**Figure 6a.** False color image of overlap region showing three types of targets.

**Figure 6b.** Anomaly output. Targets 1,2,3 detected as well as false alarms.

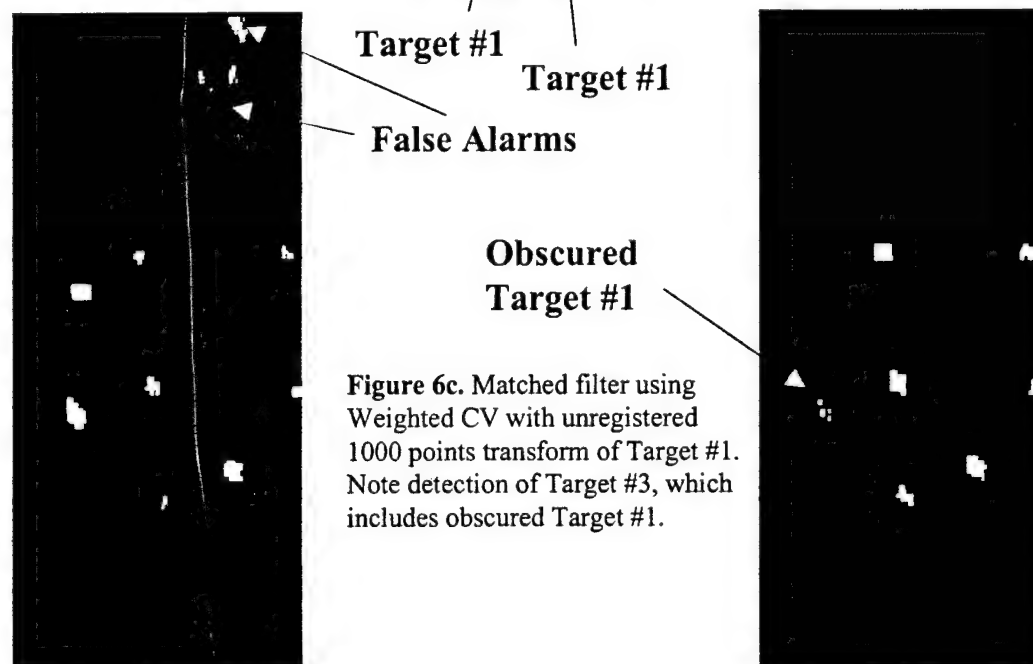


**Figure 6c.** Matched filter using Weighted CV with unregistered 1000 points transform of Target #1. Note detection of Target #3, which includes obscured Target #1.

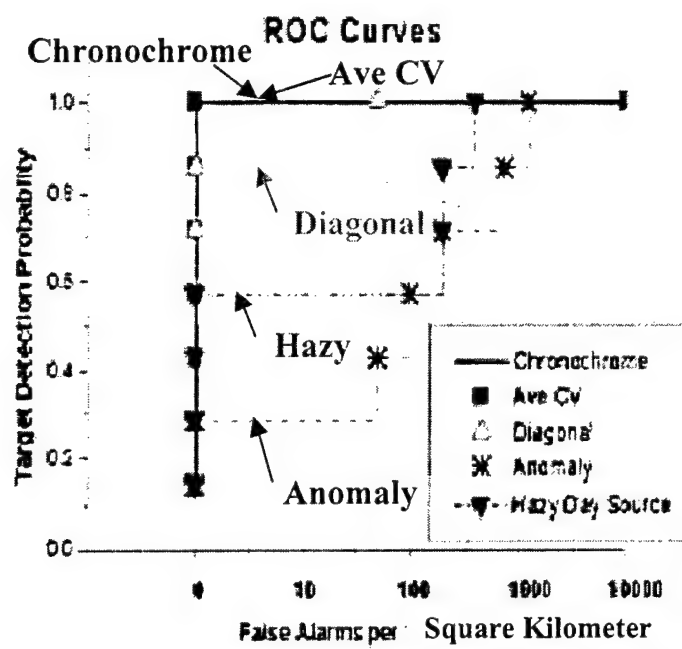


Figure 7a ROC curves using matched filter algorithm and transformed spectral signatures applied to "Hazy day" image cube. ROC curve from matched filter applied to uncorrected "Hazy Day" target #1 signature. Results from Anomaly algorithm (RX) also displayed.

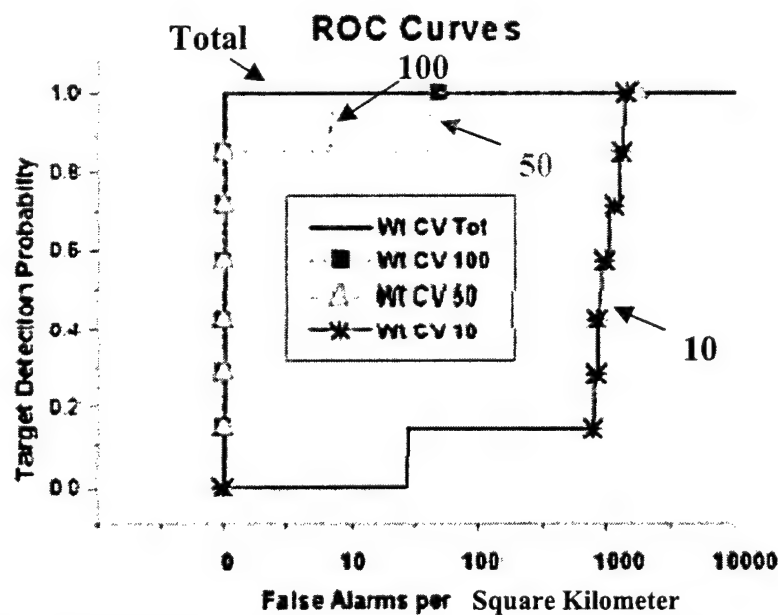


Figure 7b ROC curves for matched filter algorithm using the weighted CV transformed (10, 50, 100, all pixels in the overlap region) spectral signatures of "Hazy Day" Target #1 spectra applied to In-scene image cube.

anomaly search algorithms due to spectral library variability. Unspecific searches (such as anomaly algorithms) find spectrally uncharacteristic features in a scene, but do not distinguish military target materials from man-made objects, and do not identify materials in the scene. This work reexamined this state of affairs by transforming the hyperspectral signatures. For the particular situation examined in this study, the transformed signatures helped correctly identify significant targets, rather than only recognized non-specific aberrant objects.

The transformed and analyzed spectra were derived from particular missions flown on successive days in Florida during the autumn. However, a more rigorous test of these transforms would convert and compare spectra derived from missions flown at widely separated times and in varying seasons and backgrounds. The present study derives spectral libraries from an image cube. Other applications may instead depend on using spectral libraries from archival sources. In addition, future work may apply these approximation techniques to visible short wavelength or uncalibrated data.

## 8. ACKNOWLEDGEMENTS

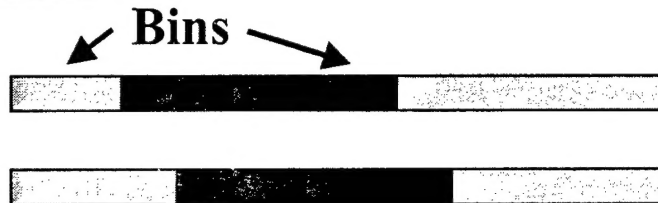
We would like to thank and acknowledge the efforts and suggestions of Frank Bucholtz, Joe Michalowicz, Al Schaum, Christopher Stellman.

## 9. REFERENCES

1. G. Hazel "Object-level change detection in spectral imagery", Accepted in IEEE Trans Geoscience Remote Sensing.
2. R. Mayer, F. Bucholtz, A. Schaum, E. Stone "Evolution of Spectral Signatures: Algorithms and assessment of transformed spectra on Matched Filter searches", Proc. National Military Sensing Symposium, Vol 44, pp. 197-212 1999.
3. R. R. Mayer, A. P. Schaum, "Target detection enhancement using temporal signature propagation," in Algorithms for Multispectral, Hyperspectral, and Ultraspectral Imagery VI, Sylvia S. Shen, Michael R. Descour, Editors, Proceedings of SPIE Vol. 4049, pp. 64-74, 2000.
4. A. Schaum, A. Stocker, "Spectral/Temporal Detection of Military Targets in Clutter", IRIS Meeting on Targets, Backgrounds, and Discrimination, Vol. 1 pp. 287-306, 1997.
5. F.A. Kruse, "Use of airborne imaging spectrometer data to map minerals associated with hydrothermally altered rocks in the Northern Grapevine Mountains, Nevada, and California," Remote Sens. Environ., vol.24, pp 31-51, 1988.
6. J.E. Conel, "Determination of surface reflectance and estimates of atmospheric optical depth and single scattering albedo from Landset Thematic Mapper data" Int. J. Remote Sensing, Vol. 11 pp. 783-828, 1990.
7. E.P. Crist, J.W. Wegrzyn, J.N. Cederquist "Automatic Scene-Adaptive target detection in hyperspectral emissive data" 2000 Meeting of Military Sensing Symposium Specialty Group on CCD, Vol 2 pp. 89-98, 2000.
8. B.C. Gao, K. Heidebrecht, and A.F.H. Goetz, "Derivation of scaled surface reflectances from AVIRIS data," Remote Sens. Environ., vol. 44 pp. 165-178, 1993.
9. G. Healey, D. Slater, "Models and methods for automated material identification in hyperspectral imagery acquired under unknown illumination and atmospheric conditions," IEEE Trans. Geoscience Remote Sens., vol 37, pp. 2706-2717, 1999.
10. S. Schweizer and J. M. F. Moura, "Hyperspectral Imagery: Clutter Adaptation in Anomaly Detection," IEEE Transactions on Information Theory, vol 46, no. 5, pp. 1855-1871, 2000.
11. L. Biehl, D.A. Landgrebe, "Effect of the Number of Samples Used in Leave-One-Out Covariance Estimator", in Algorithms for multispectral, hyperspectral, ultraspectral imagery VI, Sylvia S. Shen, Michael R. Descour, Editors, Proceedings of SPIE Vol. 4049, pp. 370-374 , 2000.
12. J.P. Hoffbeck, D.A. Landgrebe "Covariance Matrix Estimation and Classification with Limited Training Data", IEEE Transactions on Pattern Analysis and Machine Intelligence, Vol 18, 763-767, 1996.
13. S. Tadjudin , D.A. Landgrebe "Covariance Estimation with Limited Training Data", IEEE Transactions Geoscience Remote Sens., Vol 37, 2113-2118, 1999.
14. C. Stellman, F. Bucholtz, J. Michalowicz, "Dark HORSE 2 Quick-Look Report: Real-time detection of military ground targets using an infrared hyperspectral imaging sensor" NRL Technical Report, NRL/MR/5621-99-8364, April 1999.
- 15 J.A. Hackwell, D.W. Warren, R.P. Bongiovi, S.J. Hansel, T.L. Hayhurst, D.J. Mabry, M.G. Sivjee, J.W. Skinner," LWIR/MWIR imaging hyperspectral Sensor for airborne and ground-based remote sensing" in Imaging spectrometry II, Michael R. Descour, Jonathon Mooney Editors, Proceedings of SPIE Vol. 2819, pp. 102-107, 1996.
15. B.R. Johnson, "Inscene atmospheric compensation:application to SEBASS data collection at the ARM site. Part 1" Technical Report. Space and Environment Technology Center. The Aerospace Corporation. May, 1998.
16. E.P. Crist, J.W. Wegrzyn, J.N. Cederquist "Automatic Scene-Adaptive target detection in hyperspectral emissive data" 2000 Meeting of MSS Specialty Group on CCD, Vol 2 pp. 89-98, 2000.
17. I. Reed, X. Yu, "Adaptive multiple-band CFAR detection of an optical pattern with unknown spectral distribution" IEEE Trans. on Acoustics, Speech, and Sig. Proc. Vol. 38, pp. 1760-1770, 1990.
18. X. Yu, I.S. Reed, A. Stocker, "Comparative performance analysis of adaptive multispectral detectors", IEEE Trans. Signal Processing, Vol 41, 2639-2656, 1993.

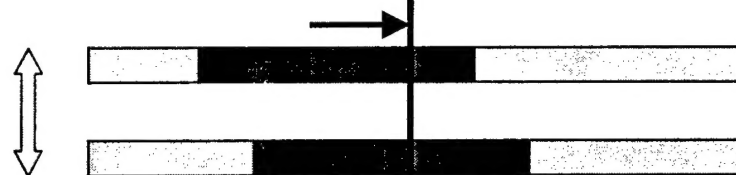
# Genetic Algorithm

## PARENTS



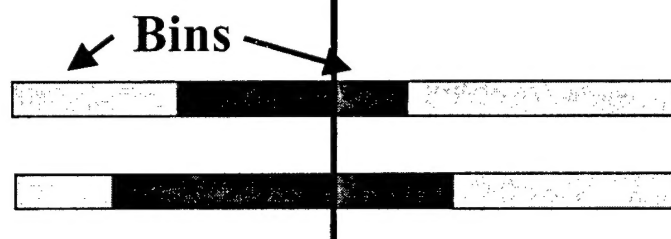
Chromosome  
(Bands)

## CROSSOVER



Chromosome  
(Bands)

## OFFSPRING



Chromosome  
(Bands)

## MUTATION

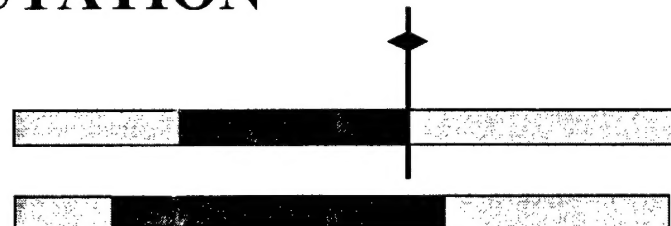


**Figure 1.** Outline of modified genetic algorithm applied to generating maximal SCR. Crossover, mutation, and offspring defined so as to fix total number of bands, but permit variable number of bands in the bins.

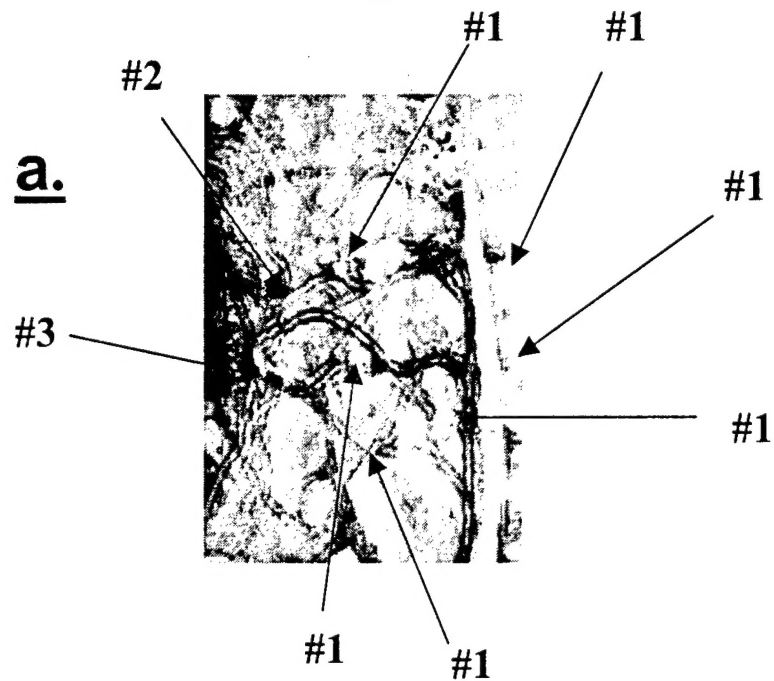


**Figure 2a.** False color image of image, background, Target #1, Target #2, Target #3.

**b.      Matched filter**



**Figure 2b.** Matched filter for Target #1 applied to In-Scene image cube.

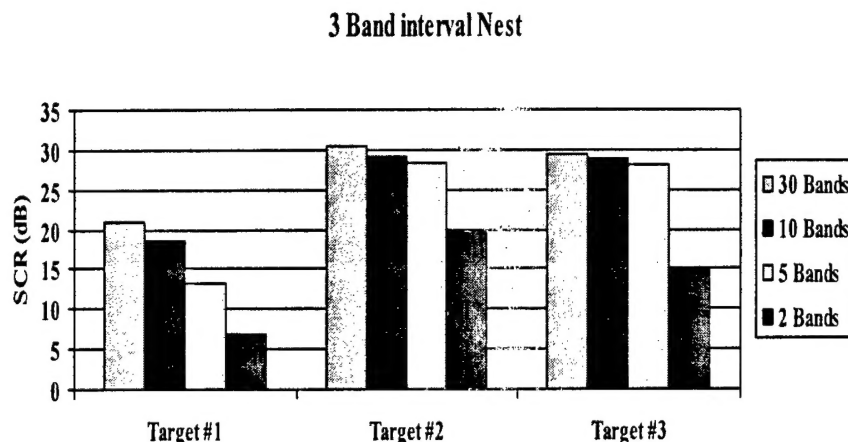


**Figure 3.** SCR of "in-scene" targets (#1,#2,#3) applied to "in-scene" imagery for 3 band interval with 30 bands (1 band separation), 10 bands (3 band separation), 5 bands (6 band separation), 2 bands (15 band separation). All selected bands have width of 1 band.

**SCR, Reference "In-Scene", Integrated**

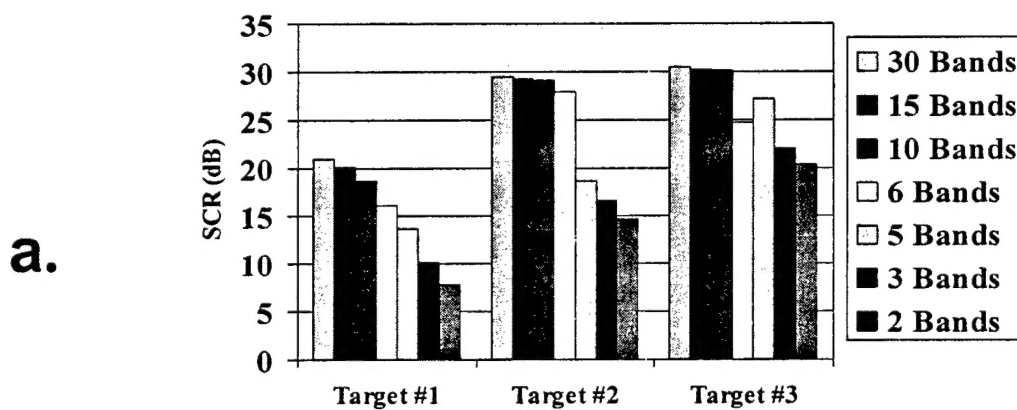


**Figure 4a.** SCR for "in-scene" targets (#1,#2,#3) applied to "in-scene" imagery using integrated bands for 30(1), 15(2), 10(3), 6(5), 5(6), 3(10), 2(15) number (width) bands.

**"Down Selected", Reference, "In-Scene"**

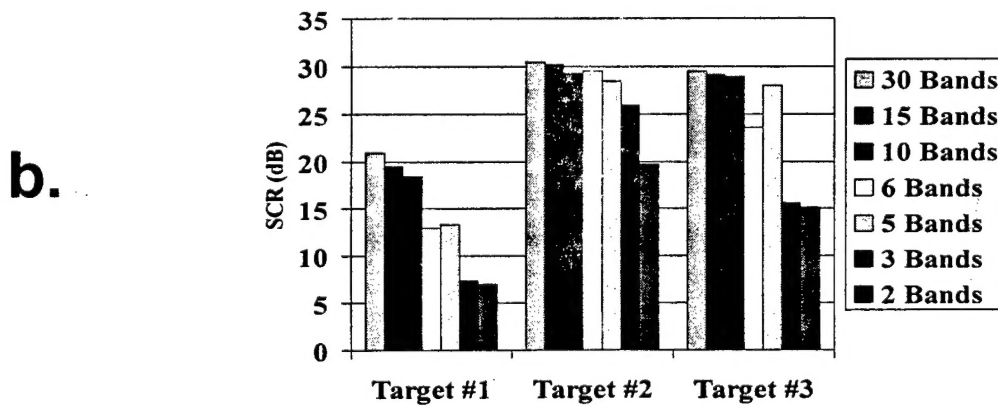


**Figure 4b.** SCR for "in-scene" targets (#1,#2,#3) applied to "in-scene" imagery "down selected" bands for 30(1), 15(2), 10(3), 6(5), 5(6), 3(10), 2(15) number (separation) bands. No band shifts.

### 5 Bands, "Down Select", Shift

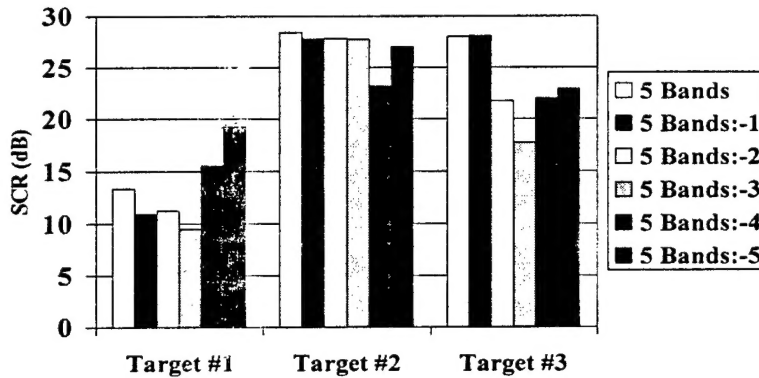


**Figure 5.** SCR for “in-scene” targets (#1,#2,#3) applied to “in-scene” imagery comparing sets of 5 bins with variable shifts or displacements.

### SCR Wt CV, Binned Bands

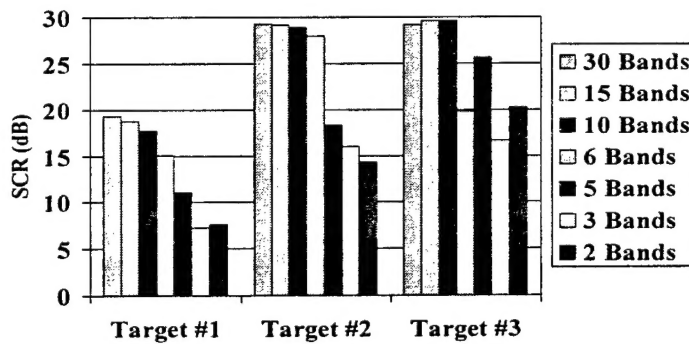


**Figure 6a.** “Hazy day” targets (#1,#2,#3) transformed to “in-scene” image conditions using the weighted CV transform. SCR for transformed targets applied to “in-scene” imagery. Transform and SCR calculation used using integrated bands for 30(1), 15(2), 10(3), 6(5), 5(6), 3(10), 2(15) number (width) bands.

### Genetic Algorithm Uniform Binned

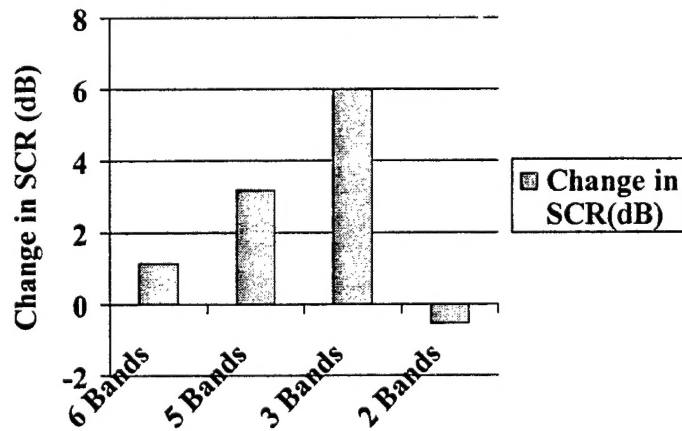


**Figure 6b.** Change in SCR for Target # 1 transformed from “hazy day” to “in-scene” using Weighted CV using genetic algorithm to choose the bands relative to uniform binning.